

Article

On the PLC Effect in a Particle Reinforced AA2017 Alloy

Markus Härtel * , Christian Illgen, Philipp Frint  and Martin Franz-Xaver Wagner 

Institute of Materials Science and Engineering, Chemnitz University of Technology, D-09107 Chemnitz, Germany; christian.illgen@mb.tu-chemnitz.de (C.I.); philipp.frint@mb.tu-chemnitz.de (P.F.); martin.wagner@mb.tu-chemnitz.de (M.F.-X.W.)

* Correspondence: markus.haertel@mb.tu-chemnitz.de; Tel.: +49-371-531-32532

Received: 15 December 2017; Accepted: 22 January 2018; Published: 25 January 2018

Abstract: The Portevin–Le Châtelier (PLC) effect often results in serrated plastic flow during tensile testing of aluminum alloys. Its magnitude and characteristics are often sensitive to a material’s heat treatment condition and to the applied strain rate and deformation temperature. In this study, we analyze the plastic deformation behavior of an age-hardenable Al-Cu alloy (AA2017) and of a particle reinforced AA2017 alloy (10 vol. % SiC) in two different conditions: solid solution annealed (W) and naturally aged (T4). For the W-condition of both materials, pronounced serrated flow is observed, while both T4-conditions do not show distinct serrations. It is also found that a reduction of the testing temperature ($-60\text{ }^{\circ}\text{C}$, $-196\text{ }^{\circ}\text{C}$) shifts the onset of serrations to larger plastic strains and additionally reduces their amplitude. Furthermore, compressive jump tests (with alternating strain rates) at room temperature confirm a negative strain rate sensitivity for the W-condition. The occurring PLC effect, as well as the propagation of the corresponding PLC bands in the W-condition, is finally characterized by digital image correlation (DIC) and by acoustic emission measurements during tensile testing. The formation of PLC bands in the reinforced material is accompanied by distinct stress drops as well as by perceptible acoustic emission, and the experimental results clearly show that only type A PLC bands occur during testing at room temperature (RT).

Keywords: serrated flow; PLC effect; dynamic strain aging; particle reinforcement; acoustic emission; jump tests; aluminum alloy

1. Introduction

Plastic instabilities, which occur in many age-hardenable aluminum alloys [1–13] within a certain regime of strain rates and testing temperatures, are often associated with the observation of repeated stress serrations in the stress–strain curves of tensile or compression tests. The so-called “jerky” or “serrated” flow is one of the most distinctive examples of plastic instability in dilute alloys. It is commonly rationalized by the dynamic interactions between solute atoms and mobile dislocations, i.e., dynamic strain aging processes [1,3–6,9,11,12,14–23]. Early observations of this phenomenon trace back to Le Châtelier who observed stress serration in the plastic flow of mild steel at elevated temperatures [24]. First studies of serrated flow in aluminum alloys were performed by Portevin and Le Châtelier [25] at ambient temperature but under different strain rates. Today, an occurrence of stress serrations in the plastic flow behavior as a result of dynamic strain aging processes is, therefore, usually referred to as the Portevin–Le Châtelier effect (PLC effect).

The PLC effect often leads to the nucleation and propagation of localized deformation bands on a macroscopic scale. Localization occurs if the local strain rate of the material exceeds the macroscopically applied strain rates during deformation [26]. A material’s susceptibility for localization is closely related to its strain rate sensitivity m : Negative strain rate sensitivities of the flow stress,

as well as a cooperative dislocation motion, are necessary requirements for the existence of a PLC effect [27–30]. Negative strain rate sensitivities of the material typically are the result of dynamic interactions between gliding dislocations and mobile solute atoms. Their interaction leads to repeating pinning and unpinning processes [14,15,31]. Therefore, local variations of mobile dislocation density increase the (negative) strain rate sensitivity. However, many other parameters can also influence the magnitude of an actual PLC effect: the chemical composition, the amount and type of solute atoms, texture, grain size, strain hardening rate, heat treatment condition, and especially strain rate as well as temperature [3,16,18,21,32]. Serrated plastic flow may also influence formability: PLC effects in sheet metal forming lead, e.g., to an optical degradation (strain marks). In extrusion, PLC effects lead to a reduced formability, but with thermal suppression of those deformation bands, those negative aspects of localized plastic flow can be reduced [10,32].

In this paper, we study the influence of different heat treatments, deformation temperatures and applied strain rates on the magnitude of a potential PLC effect in a high-strength, age-hardenable Al-Cu alloy (AA2017), and in a particle reinforced AA2017 alloy (10 vol. % SiC) in two different conditions. Studies on the general mechanical properties, the deformation behavior and the accompanying microstructural aspects have been the focus of recent research efforts [10,33,34]. The influence of a finely dispersed and homogeneously distributed particle reinforcement on the occurrence and magnitude of PLC effects, however, has not been studied in detail so far. The present study documents in detail that a PLC effect only occurs in solution annealed conditions, and that a reduced testing temperature leads to a suppression of PLC band formation.

2. Materials and Methods

The mechanical behavior of two different age-hardenable alloys was studied in this work. The chemical compositions (wt. %) of the examined AA2017 alloy as well as of the particle reinforced AA2017 alloy (with 10 vol. % SiC; particle size less than 2 μm) are given in Table 1. Both materials were obtained as commercial, gas-atomized, spherical powders with a particle size below 100 μm [35]. The powders were milled for about 4 h in a high energy ball mill (Simoloyer1 CM08 by Zoz GmbH, Wenden, Germany), followed by hot isostatic pressing (HIP) at 450 $^{\circ}\text{C}$ for 3 h and at a pressure of 1100 bar [35]. Semi-finished products were then generated by extrusion of the mixed powders to billets with a square cross-section of 15 \times 15 mm^2 . Further details on the fabrication procedures and particularly on the morphology and on the homogeneous spatial distribution of the reinforcing particles are given in [35]. For characterization of the thermo-mechanical behavior and of the strain rate sensitivity, cylindrical tensile samples (with a gauge length of 10.5 mm and a diameter of 3.5 mm) and cylindrical compression specimens (with an aspect ratio of one, diameter 5 mm) were machined from the billets parallel to the extrusion direction.

Table 1. Chemical composition of the age-hardenable Al-Cu alloy AA2017 and of the particle reinforced AA2017 composite material (with 10 vol. % SiC). The base compositions of both materials (i.e., of the alloy vs. the matrix-forming alloy of the composite) are very similar, allowing for a direct comparison of the mechanical behavior.

Element	Cu	Mg	Mn	Fe	Si	Cr	Ni	Ti	Zn	Al
AA2017 Content in wt. %	3.83	0.71	0.64	0.17	0.065	0.017	0.0049	0.0025	<0.00100	bal.
AA2017 (10 vol. % SiC) Content in wt. %	3.81	0.68	0.49	0.27	8.26	0.010	0.016	0.016	0.11	

As observed in previous studies [6,16,32,36], different heat treatment conditions can strongly affect the occurrence and magnitude of PLC effects. In order to provide a well-defined heat treatment condition, the materials were heat treated to generate two conditions: solid solution annealed (W) and naturally aged (T4). For the W-condition, the material was solid solution annealed for 120 min at 505 $^{\circ}\text{C}$ and quenched in ice water. To suppress further natural aging processes prior to mechanical

testing, all specimens were stored in liquid nitrogen (at $-196\text{ }^{\circ}\text{C}$) after the heat treatment. The naturally aged condition (T4) was solution annealed with the same parameters and subsequently naturally aged at room temperature (RT) for two weeks [35].

To characterize the deformation behavior of both materials, we performed strain-controlled uniaxial tensile tests (Zwick/Roell 20 kN tensile testing machine, Ulm, Germany) for both conditions W and T4. For all tensile tests, the temperature was RT and the strain rate was 10^{-3} s^{-1} . Besides the heat treatment condition, the applied strain rate governs a potential PLC effect. Particularly a negative strain rate sensitivity increases the potential of the occurrence of PLC effects [1,2,4,5,15,32,37,38]. In order to characterize the susceptibility of both materials to strain localization, we therefore also performed strain-controlled uniaxial compression tests (Zwick/Roell 20 kN tensile testing machine, Ulm, Germany) at RT with a sudden change of strain rate (jump tests). During those jump tests, the strain rate was repeatedly changed by one order of magnitude. The applied strain rates were in a range from 10^{-5} s^{-1} to 10^{-2} s^{-1} for the both investigated material conditions. The strain rate sensitivity value m was then determined from the true stress-strain curves by evaluating stress increments at the points of strain rate changes:

$$m = \frac{\Delta \ln \sigma}{\Delta \ln \dot{\epsilon}} = \frac{\ln \sigma_2 - \ln \sigma_1}{\ln \dot{\epsilon}_2 - \ln \dot{\epsilon}_1} . \quad (1)$$

In Equation (1), $\dot{\epsilon}_1$ is representing the strain rate immediately prior to, and $\dot{\epsilon}_2$ the strain rate immediately after, the change of strain rate. The values for σ_1 and σ_2 are the corresponding true stresses approximated by the application of tangents to the regions of constant strain rate.

Since testing temperature has a considerable influence on the magnitude of serrated flow [32], the uniaxial tensile tests were performed at different temperatures (RT, $-60\text{ }^{\circ}\text{C}$, and $-196\text{ }^{\circ}\text{C}$) at a constant strain rate of 10^{-3} s^{-1} . A special double-ring cooling device placed around the tensile specimen was used to adjust testing temperatures below RT, Figure 1. For testing temperatures of $-60\text{ }^{\circ}\text{C}$, the inner ring of the device was filled with n-pentane (C_5H_{12}) until the specimen was completely immersed, Figure 1b. Cooling was performed by adding liquid nitrogen into the outer ring of the device. For the testing temperature of $-196\text{ }^{\circ}\text{C}$, both chambers of the cooling device were filled with liquid nitrogen. Using a thermocouple (type K), the testing temperatures were controlled in situ. The thermocouple was located directly on the surface of the specimens. Strain values during these tests were determined from the crosshead displacement data of the tensile testing machine.

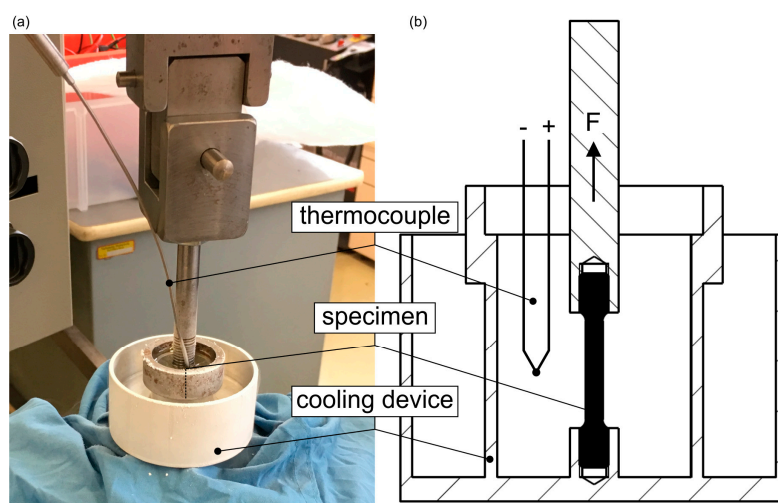


Figure 1. Experimental setup applied for tensile tests at different temperatures below room temperature (RT) as (a) photograph, and (b) as schematic drawing. The setup consists of a special double-ring cooling device surrounding the tensile specimen. The testing temperature is measured with a thermocouple placed on the sample surface.

Localized deformation can be documented by diffraction methods, 2D or 3D local strain mapping as well as by infrared thermal imaging methods [39–44]. In the present study, the local deformation behavior of the investigated material conditions was characterized in greater detail by additional tensile tests in combination with digital image correlation (DIC). DIC allows the documentation and analysis of the nucleation as well as the propagation of macroscopic deformation bands resulting from PLC effects by recording surface displacement fields and the corresponding strain maps. A fine speckle pattern for image analysis was produced on the sample surfaces using a graphite spray (a close-up view of the sample surface is shown in the video provided as supplementary material Video S1: Video S1: PLC effect reinforced AA2017 using DIC and AE). Finally, a highly sensitive unidirectional stereo microphone (XYH-6 X/Y Capsule by Zoom™, Hauppauge, NY, USA, 24 bit, up to 96 kHz) was used in the same setup (Figure 2) to measure acoustic emission signals (as integral acoustic intensity) based on earlier reports on acoustic emission related to PLC effects [2,3,15,18,45–47].

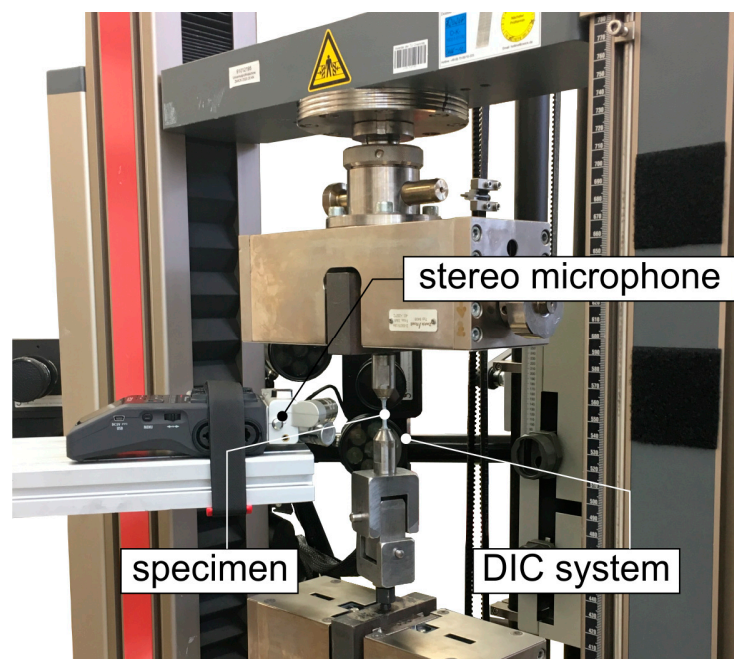


Figure 2. Experimental setup for digital image correlation (DIC) observations used during tensile testing. In addition to the optical measurement components, a highly sensitive unidirectional stereo microphone was used to measure the acoustic emission associated with The Portevin–Le Châtelier (PLC) effects.

3. Results and Discussion

Figure 3 shows tensile (engineering) stress-strain curves of both materials in the W- and T4-conditions. The data show that, as expected, both particle reinforcements and aging increase the strength of the material. In contrast to the T4-condition, the W-condition exhibits the typical serrated flow (PLC effect) for both materials. PLC effects are strongly influenced by the concentration of solute atoms (chemical composition and aging condition). Aging of aluminum alloys leads to precipitation, which considerably reduces the number of solute atoms. As a consequence, the formation of PLC bands is suppressed or delayed towards higher strains for the naturally aged condition T4 in Figure 3. This result is in good agreement with the results found in [3,6,16,32,48]. Another important finding is the different onset strain of the serrated flow for both materials: The plastic strain associated with the formation of the first PLC band is 6.5% for the AA2017 base material, but only 1.9% for the reinforced material. The onset of the PLC effect in the stress-strain curve is typically attributed to a necessary density of defects (basically dislocations and vacancies) that is

required for dynamic strain aging [3,6,7,49–53]. Hence, an initial concentration of defects introduced by either quenching or by early plastic deformation is required to increase diffusion rates of the solute atoms and thus to trigger dislocation pinning. As discussed in [14,48], an earlier occurrence of stress serrations in the particle reinforced material (Figure 3) is in good agreement with this interpretation: The particle/matrix interfaces and the stress fields surrounding the particles locally lead to a rapid increase of the dislocation density [33] during plastic deformation. This increased number of defects allows for faster pipe diffusion processes [54–57] and—for the material studied here—accelerates dynamic strain aging at lower strain values. The extent of this effect likely depends on the volume fraction and the spatial arrangement of the dispersed particles [14,48].

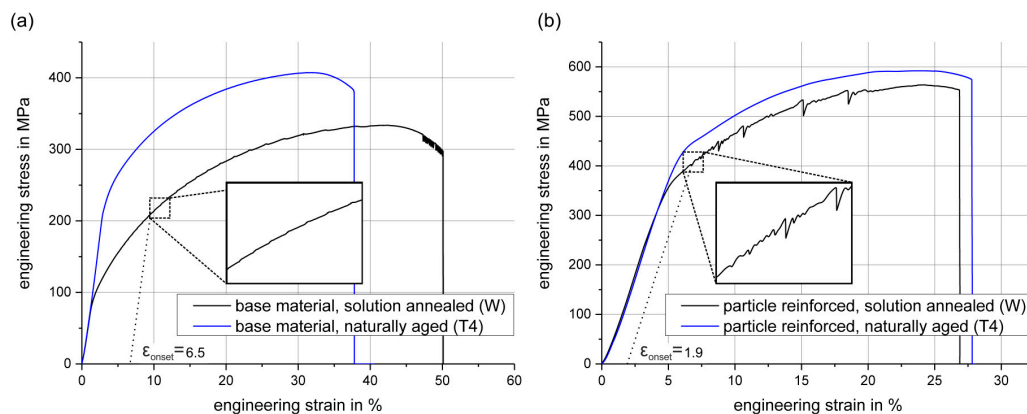


Figure 3. Stress-strain curves of (a) the AA2017 base material in the solution annealed condition W and in the naturally aged condition T4, and (b) of the particle reinforced AA2017 material in solution annealed condition W and in naturally aged condition T4. Only the W-conditions exhibit serrated flow. In the inset with a higher magnification, type A PLC serrations can be observed.

It is clear from Figure 3 that the characteristics of the serrations (i.e., the “shapes” of peaks and drops in the stress-strain curves) caused by localized deformation clearly differ in the two materials. Based on the characteristics of serrations, different types of PLC bands can be classified; the most common terminology distinguishes three different types [14,22,28,58,59]. Type A is characterized by repeated nucleation of single bands that move continuously from one side of the gauge length through the entire specimen. The corresponding stress-strain curves typically show a sudden increase, followed by a drop below the original stress level. Type B PLC bands are quickly arrested after nucleation; instead of widespread propagation, new bands are formed in the direct vicinity of the arrested bands. The stress-strain signal shows rapid serrations that oscillate around the original stress level. Type C PLC bands are associated with nucleation of randomly located bands within the gauge length and show repeated drops below the stress level followed by non-linear stress increases. For both AA2017 and AA2017 (10 vol. % SiC), we observed type A PLC bands in W-condition, see the higher magnification inset of Figure 3. The amplitudes of the serrations in Figure 3a (base material) are not as pronounced as in the inset in Figure 3b (particle reinforced material). This may be attributed to the stress fields of the particles, which represent obstacles for dislocation motion and thus increase the pinning effect. Between each large stress drop and the next pronounced serration in Figure 3b, we also observe additional serrated flow with lower amplitudes. These second-order serrations might, in theory, indicate the additional formation of type B PLC bands. However, such bands could not be recorded by our DIC observations. Therefore, we conclude that the propagation of the observed PLC bands (type A) is stopped temporarily by the stress fields of individual or clusters of several. This leads to additional pinning on the macro-scale (i.e., pinning of the propagating band as opposed to pinning of individual dislocations). We note that the amplitude of stress-strain serrations may also

be influenced by the stiffness of the testing device, by the geometry of the specimen and by the surface quality of the specimen [8,17,21,45].

Figure 4 shows the results of the (compressive) jump tests of both materials in the solution annealed condition (W). The green and blue curves illustrate the true stress-true strain data (which are required for determining m -values) of the base material and of the particle reinforced material, respectively. In a range from 10^{-5} s^{-1} to 10^{-2} s^{-1} both materials exhibit a positive stress overshoot immediately after each strain rate jump. This stress reaction to strain rate jumps is generally referred to as instantaneous strain rate sensitivity [5,13,14,38,60] and is usually followed by a transient period of stress before the flow stress reaches a new steady state. This instantaneous strain rate sensitivity always takes positive values and can be rationalized with the time-dependence of the solute concentration near mobile dislocations [36]. However, after reaching the steady state, the true stress-true strain curves exhibit a different behavior: In the range from 10^{-5} s^{-1} to 10^{-2} s^{-1} both materials actually respond with decreasing flow stresses when the strain rate is increased. Consequently, a decrease of the strain rate leads to an increase of the flow stress after each jump for both materials. From this behavior, a negative strain rate sensitivity for both materials in the W-condition is determined (see Table 2). For all jumps from low strain rates to high strain rates, negative strain rate sensitivity values m were calculated. With the negative strain rate sensitivity factors m for both materials a necessary requirement for the occurrence of PLC effects is fulfilled [27–30].

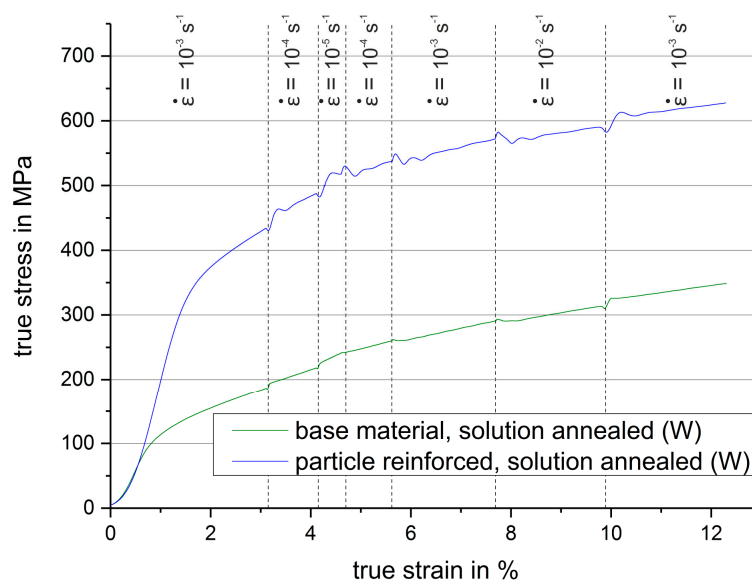


Figure 4. True stress-true strain curves measured in compressive jump tests with strain rates ranging from 10^{-5} s^{-1} to 10^{-2} s^{-1} for both materials in the solution annealed condition (W). When strain rates are reduced (first jumps and final jump), flow stresses are increased; an increase of the strain rate (intermediate jumps) leads to decreasing flow stresses. This clearly indicates that both materials exhibit a negative strain rate sensitivity.

Table 2. Strain rate sensitivity m , determined from different strain rate jumps for solution annealed AA 1070 (base material and particle reinforced alloy). All data represent are arithmetically averaged parameters (\pm standard deviations) from at least three similar tests.

Strain Rate Jump in s^{-1}	10^{-5} to 10^{-4}	10^{-4} to 10^{-3}	10^{-3} to 10^{-2}
True Strain in%	4.61	5.62	7.68
m base material	-0.0044 ± 0.0006	-0.0083 ± 0.0006	-0.0105 ± 0.0011
m reinforced	-0.0231 ± 0.0004	-0.0062 ± 0.0034	-0.0060 ± 0.0001

The results of additional jump tests with alternating strain rates (between 10^{-3} s^{-1} and 10^{-2} s^{-1}) shown in Figure 5a confirms the negative strain rate sensitivity. Again, both materials exhibit the typical instantaneous (overshoot) strain rate sensitivity for all conditions (W and T4). The stress overshoot for the reinforced conditions is much higher than for the base material. Figure 5b shows the strain rate sensitivity values plotted versus true strain calculated from the jumps of stress-strain curves shown in Figure 5a. The results of both W-conditions again highlight that an increased strain rate leads to decreasing flow stresses. Interestingly, in case of both T4-conditions, a negative strain rate sensitivity was observed, too. However, the absolute m -values of these conditions are considerably smaller compared to the values determined for the W-conditions. We also note that absolute m -values exhibit a tendency to decrease with increasing plastic strain. This decrease is assumed to originate from aging during compressive testing as already reported in [2,4,5,32] (and for AMCs in [9]). Moreover, a decrease of absolute values of negative strain rate sensitivity is in good agreement with the absence of serrated flow (PLC effect) for the naturally aged condition (T4) in the tensile tests at RT mentioned above.

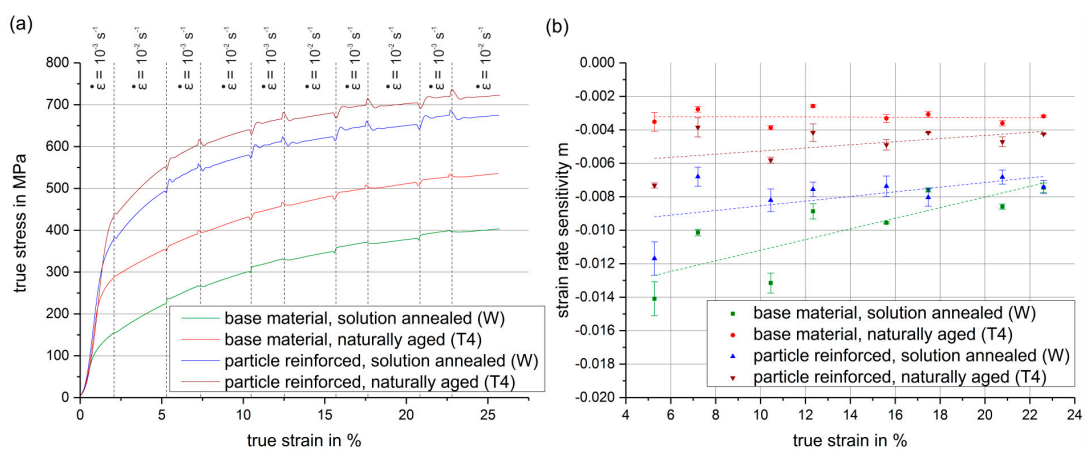


Figure 5. Compression tests with alternating strain rates between 10^{-3} s^{-1} and 10^{-2} s^{-1} . (a) True stress-true strain curves of jump tests for both materials in solution annealed (W) and naturally aged condition (T4). (b) Strain rate sensitivity m versus true strain calculated from the true stress-true strain curves in a).

For the discussion of the influence of temperature on PLC effects, the results of the tensile tests performed at $-60 \text{ }^\circ\text{C}$ and $-196 \text{ }^\circ\text{C}$ and at a constant strain rate (10^{-3} s^{-1}) of the base material (in conditions W and T4) are presented in Figure 6. Figure 6a shows a reduction of stress serrations for the solution annealed condition W compared to the tensile tests at RT (see Figure 3a). Additionally, the critical strain for the onset of serrated flow in the W-condition is shifted to a larger engineering strain value of 11.3%. The T4-condition of the base material does not exhibit any serrations at $-60 \text{ }^\circ\text{C}$. At a testing temperature of $-196 \text{ }^\circ\text{C}$ (Figure 6b) the stress-strain curve of the W-condition does not show pronounced serrations; a slight waviness of the stress signal is most likely related to film boiling of the liquid nitrogen. A critical strain for the onset of stress serrations cannot be determined reliably for the W-condition. For the T4-condition, again, no serrations are observed.

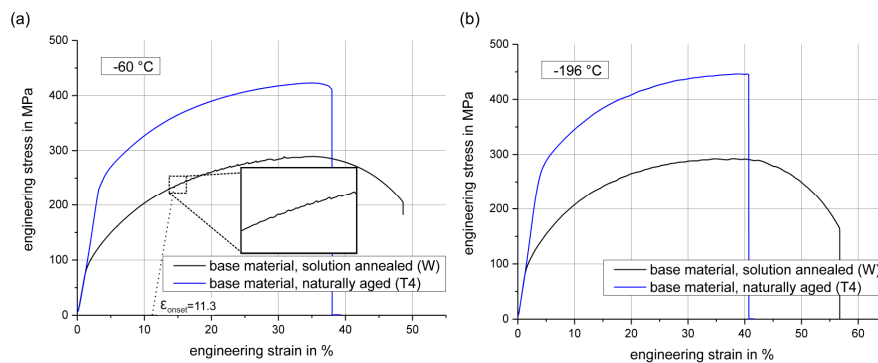


Figure 6. Tensile engineering stress-strain curves measured at low temperatures. (a) AA2017 base material in solution annealed condition W and in naturally aged condition T4 at $-60\text{ }^{\circ}\text{C}$. (b) AA2017 base material in solution annealed condition W and in naturally aged condition T4 at $-196\text{ }^{\circ}\text{C}$. Only the W-conditions still exhibit a slightly serrated flow associated with the PLC effect (inset at higher magnification). The serrations decrease with decreasing testing temperature.

Figure 7 shows the results of low-temperature tensile testing of the particle reinforced material for both conditions (W and T4). As already found for the base material (see Figure 6), the particle reinforced material in Figure 7a shows a significant decrease of serrated flow at $-60\text{ }^{\circ}\text{C}$ compared to RT (see Figure 3b). Again, the critical strain for the onset of stress serrations in the W-condition is shifted to larger strain values of about 7.0% compared to 1.9% at RT. At $-60\text{ }^{\circ}\text{C}$, stress serrations are already completely suppressed for the T4-condition. Figure 7b shows a similar characteristic of stress-strain behavior compared to the behavior of the base material shown in Figure 6b. Lower testing temperatures ($-196\text{ }^{\circ}\text{C}$) lead to a reduction of serrations in the stress-strain curve for the W-condition compared to testing at RT (see Figure 3b). Again, the critical strain for the onset of stress serrations cannot be determined clearly. For the T4-condition, an absence of serrations is observed, i.e., the PLC effect is completely suppressed. In summary, the suppression of serrated flow at lower temperatures ($-60\text{ }^{\circ}\text{C}$ and $-196\text{ }^{\circ}\text{C}$, Figures 6 and 7) clearly indicates that thermally activated and diffusion-controlled processes are primarily responsible for serrated flow at RT in the materials studied here, irrespective of whether they contain particles (which tend to increase stress amplitudes during serrated flow) or not. Temperature reduction leads to reduced diffusivity of the solute atoms and thus to a lower efficiency of dynamic strain aging processes in the AA2017 alloy.

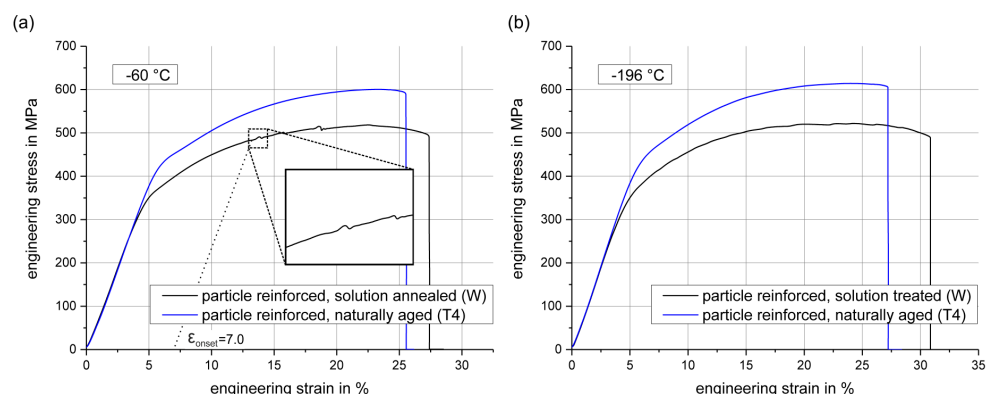


Figure 7. Tensile engineering stress-strain curves at low temperatures. (a) Particle reinforced AA2017 material in the solution annealed (W) and naturally aged (T4) conditions at $-60\text{ }^{\circ}\text{C}$. (b) Particle reinforced AA2017 material in solution annealed (W) and naturally aged (T4) conditions at $-196\text{ }^{\circ}\text{C}$. Only the W-conditions exhibit some serrated flow (inset at higher magnification). PLC effects are reduced by decreasing the testing temperature.

Additional experiments were performed to further study the material condition that exhibits the most pronounced PLC effect, particle reinforced AA2017 in W-condition. Simultaneous DIC and acoustic emission measurements were performed during uniaxial tensile tests at RT. Representative results of these tensile tests are shown in Figure 8. Figure 8a shows the evolution of stress, strain and of the acoustic emission signal as a function of time. In this figure, “macroscopic” strain represents the average uniaxial strain value across the entire surface area that was evaluated by DIC. Both stress and strain signals clearly indicate serrated flow; stress drops coincide with positive jumps of macroscopic strain. The acoustic emission signal is represented by the black line in Figure 8a (the signal simply represents the integral acoustic intensity). Each distinct stress drop is also accompanied by perceptible acoustic emission, see also the video provided as supplementary material (Video S1: PLC effect reinforced AA2017 using DIC and AE). The DIC observations show that the measured acoustic emission is clearly associated with the nucleation of a separate deformation band in the material, which is accompanied by a distinct stress drop at the same moment as band nucleation provides a sudden increase in local strain and thus partially elastically unloads the tensile sample. In Figure 8b, the nucleation and two stages during the propagation of one representative deformation band are shown as DIC-derived strain maps, where strain values correspond to uniaxial tensile strains determined in the (loading) x -direction. These characteristic situations are marked in the stress curve of Figure 8a (A,B,C). The nucleation (A) of a single deformation band at the lower end of the gauge length accompanied by a distinct stress drop can be clearly identified. Further deformation proceeds by propagation (B) of the single band across the gauge length. This is accompanied by very small serrations of the stress signal, most likely due to dislocation particle interactions at the reaction front of the deformation band [42]. Interestingly, no secondary PLC band nucleation is observed, confirming that the PLC effect observed here is not of type B. Immediately prior to the next distinct stress drop (accompanied by the nucleation of a new deformation band) the current PLC band reaches the opposite end of the gauge length (C). This process occurs repeatedly during tensile deformation until final fracture. The combination of DIC and acoustic emission provides detailed information on nucleation events and on the propagation of individual PLC bands. Acoustic emission may even contribute to an analysis of the microstructural interaction of the growing band with the material’s reinforcement particles, which is the subject of ongoing work.

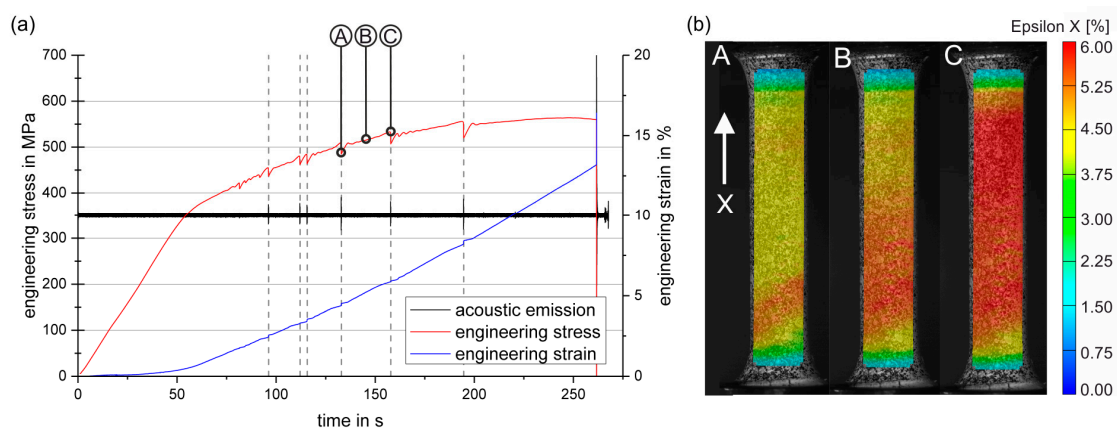


Figure 8. (a) Engineering stress, engineering strain and acoustic emission signal (the signal simply represents the integral acoustic intensity) as a function of testing time during uniaxial tensile testing of the particle reinforced material (W-condition) at RT. The stress signal (red) shows distinct stress-drops accompanied by strain discontinuities (blue curve) and a perceptible acoustic emission (black curve). (b) Strain fields measured by DIC (uniaxial tensile strain maps) at different stages of the evolution of a single PLC band (type A): Nucleation (A) and propagation (B to C) of a single deformation band.

4. Summary and Conclusions

Serrated flow was investigated in an age-hardenable Al-Cu alloy AA2017 and in a particle reinforced AA2017 alloy (10 vol. % SiC) as a function of heat treatment condition, applied strain rate, as well as testing temperature. Two different heat treatment conditions were analyzed: solid solution annealed (W) and naturally aged (T4). It was found that both materials exhibit a typical serrated flow in the W-condition during tensile testing at ambient temperature. Furthermore, a difference in the plastic strain onset of the initiation of serrated flow was observed. An earlier onset occurs in the particle reinforced material, which can be attributed to an accelerated dynamic strain aging due to a comparatively faster increase of dislocation density during plastic deformation. We also documented a negative strain rate sensitivity during compressive jump tests from 10^{-5} s^{-1} to 10^{-2} s^{-1} for both materials and both conditions. The (negative) strain rate sensitivity values determined for the T4-conditions show considerably lower absolute values compared to the W-condition. This is in line with the observation of a reduced serrated flow (PLC effect) for the naturally aged condition (T4) in tensile tests at RT.

During tensile tests at lower deformation temperatures ($-60 \text{ }^{\circ}\text{C}$, $-196 \text{ }^{\circ}\text{C}$), a shift of the critical strain values for the onset of serrated flow in the W-condition to larger strain values and a decreased amplitude of stress fluctuations were observed. Serrated flow is completely suppressed at lower temperatures for T4-condition. The temperature-dependence of serrated flow in both materials reveals that thermally activated and diffusion-controlled processes are the main reason for the different flow behavior of the materials at RT, $-60 \text{ }^{\circ}\text{C}$, and $-196 \text{ }^{\circ}\text{C}$. The nucleation and propagation of single PLC bands were characterized using DIC and acoustic emission measurements for the condition with the most pronounced PLC effect (particle reinforced AA2017 in W-condition). DIC strain maps confirm that the PLC bands are of type A. Acoustic emission data can be directly related to nucleation events of distinct bands.

Supplementary Materials: The following are available online at www.mdpi.com/2075-4701/8/2/88/s1, Video S1: PLC effect reinforced AA2017 using DIC and AE.

Acknowledgments: The authors gratefully acknowledge funding by the German Research Foundation (Deutsche Forschungsgemeinschaft, DFG) through the Collaborative Research Center SFB 692 (projects A2 and C5). We also thank our partners in project A2, Daisy Julia Nestler, and Steve Siebeck, for fabrication of the reinforced materials.

Author Contributions: Markus Härtel and Christian Illgen conceived and designed the experiments. Christian Illgen performed and analyzed the experiments, prepared the figures. Markus Härtel and Christian Illgen drafted the manuscript. Philipp Frint and Martin Franz-Xaver Wagner discussed the results and analysis and helped writing the manuscript.

Conflicts of Interest: The authors declare no conflict of interest.

References

1. Böhlke, T.; Bondár, G.; Estrin, Y.; Lebyodkin, M.A. Geometrically non-linear modeling of the Portevin-Le Chatelier effect. *Comput. Mater. Sci.* **2009**, *44*, 1076–1088. [[CrossRef](#)]
2. Chmelík, F.; Pink, E.; Król, J.; Balík, J.; Pešička, J.; Lukáč, P. Mechanisms of serrated flow in aluminium alloys with precipitates investigated by acoustic emission. *Acta Mater.* **1998**, *46*, 4435–4442. [[CrossRef](#)]
3. Delaunois, F.; Denil, E.; Marchal, Y.; Vitry, V. Accelerated aging and Portevin-Le Chatelier effect in AA 2024. *Mater. Sci. Forum* **2017**, *879*, 524–529. [[CrossRef](#)]
4. Gupta, S.; Beaudoin, A.J.; Chevy, J. Strain rate jump induced negative strain rate sensitivity (NSRS) in aluminum alloy 2024: Experiments and constitutive modeling. *Mater. Sci. Eng. A* **2017**, *683*, 143–152. [[CrossRef](#)]
5. Jiang, H.; Zhang, Q.; Chen, X.; Chen, Z.; Jiang, Z.; Wu, X.; Fan, J. Three types of Portevin-Le Chatelier effects: Experiment and modelling. *Acta Mater.* **2007**, *55*, 2219–2228. [[CrossRef](#)]
6. Jiang, H.; Zhang, Q.; Wu, X.; Fan, J. Spatiotemporal aspects of the Portevin-Le Chatelier effect in annealed and solution-treated aluminum alloys. *Scr. Mater.* **2006**, *54*, 2041–2045. [[CrossRef](#)]

7. Jiang, Z.; Zhang, Q.; Jiang, H.; Chen, Z.; Wu, X. Spatial characteristics of the Portevin-Le Chatelier deformation bands in Al-4 at%Cu polycrystals. *Mater. Sci. Eng. A* **2005**, *403*, 154–164. [[CrossRef](#)]
8. Rashkeev, S.N.; Glazov, M.V.; Barlat, F. Strain-rate sensitivity limit diagrams and plastic instabilities in a 6xxx series aluminum alloy. Part I: Analysis of temporal stress-strain serrations. *Comput. Mater. Sci.* **2002**, *24*, 295–309. [[CrossRef](#)]
9. Serajzadeh, S.; Ranjbar Motlagh, S.; Mirbagheri, S.M.H.; Akhgar, J.M. Deformation behavior of AA2017-SiCp in warm and hot deformation regions. *Mater. Des.* **2015**, *67*, 318–323. [[CrossRef](#)]
10. Wagner, S.; Härtel, M.; Frint, P.; Wagner, M.F.X. Influence of ECAP on the formability of a particle reinforced 2017 aluminum alloy. *J. Phys. Conf. Ser.* **2017**, *755*, 11001. [[CrossRef](#)]
11. Xiang, G.F.; Zhang, Q.C.; Liu, H.W.; Wu, X.P.; Ju, X.Y. Time-resolved deformation measurements of the Portevin-Le Chatelier bands. *Scr. Mater.* **2007**, *56*, 721–724. [[CrossRef](#)]
12. Zhang, Q.; Jiang, Z.; Jiang, H.; Chen, Z.; Wu, X. On the propagation and pulsation of Portevin-Le Chatelier deformation bands: An experimental study with digital speckle pattern metrology. *Int. J. Plast.* **2005**, *21*, 2150–2173. [[CrossRef](#)]
13. Zhang, S.; McCormick, P.G.; Estrin, Y. The morphology of Portevin-Le Chatelier bands: Finite element simulation for Al-Mg-Si. *Acta Mater.* **2001**, *49*, 1087–1094. [[CrossRef](#)]
14. Dierke, H.; Krawehl, F.; Graff, S.; Forest, S.; Šachl, J.; Neuhäuser, H. Portevin-Le Chatelier effect in Al-Mg alloys: Influence of obstacles-experiments and modelling. *Comput. Mater. Sci.* **2007**, *39*, 106–112. [[CrossRef](#)]
15. Chmelík, F.; Klose, F.B.; Dierke, H.; Šachl, J.; Neuhäuser, H.; Lukáč, P. Investigating the Portevin-Le Chatelier effect in strain rate and stress rate controlled tests by the acoustic emission and laser extensometry techniques. *Mater. Sci. Eng. A* **2007**, *462*, 53–60. [[CrossRef](#)]
16. Liang, S.; Qing-Chuan, Z.; Peng-Tao, C. Influence of solute cloud and precipitates on spatiotemporal characteristics of Portevin-Le Chatelier effect in A2024 aluminum alloys. *Chin. Phys. B* **2009**, *18*, 3500–3507. [[CrossRef](#)]
17. Lebedkina, T.A.; Lebyodkin, M.A. Effect of deformation geometry on the intermittent plastic flow associated with the Portevin-Le Chatelier effect. *Acta Mater.* **2008**, *56*, 5567–5574. [[CrossRef](#)]
18. Grzegorzczak, B.; Ozgowicz, W.; Kalinowska-Ozgowicz, E.; Kowalski, A. Investigation of the Portevin-Le Chatelier effect by the acoustic emission. *J. Achiev. Mater. Manuf. Eng.* **2013**, *60*, 7–14.
19. Cottrell, A.H. LXXXVI. A note on the Portevin-Le Chatelier effect. *Lond. Edinb. Dublin Philos. Mag. J. Sci.* **1953**, *44*, 829–832. [[CrossRef](#)]
20. Robinson, J.M.; Shaw, M.P. Microstructural and mechanical influences on dynamic strain aging phenomena. *Int. Mater. Rev.* **1994**, *39*, 113–122. [[CrossRef](#)]
21. Yilmaz, A. The Portevin-Le Chatelier effect: A review of experimental findings. *Sci. Technol. Adv. Mater.* **2011**, *12*, 063001. [[CrossRef](#)] [[PubMed](#)]
22. Rodriguez, P.; Venkadesan, S. Serrated Plastic Flow Revisited. *Solid State Phenom.* **1995**, *42–43*, 257–266. [[CrossRef](#)]
23. Rizzi, E.; Hähner, P. On the Portevin-Le Chatelier effect: Theoretical modeling and numerical results. *Int. J. Plast.* **2004**, *20*, 121–165. [[CrossRef](#)]
24. Le Chatelier, A. Influence du temps et de la température sur les essais au choc. *Rev. Met. Paris* **1909**, *6*, 914–917. [[CrossRef](#)]
25. Portevin, A.; Le Chatelier, F. Sur un phénomène observé lors de l'essai de traction d'alliages en cours de transformation. *Comptes Rendus Acad. Sci. Paris* **1923**, *176*, 507–510.
26. Considère, M. Memoire sur l'emploi du fer et de l'acier dans les constructions. *Ann. Ponts Chaussees* **1885**, *9*, 574–775.
27. Hähner, P. On the physics of the Portevin-Le Chatelier effect part 1: The statistics of dynamic strain ageing. *Mater. Sci. Eng. A* **1996**, *207*, 208–215. [[CrossRef](#)]
28. Hähner, P. On the physics of the Portevin-Le Chatelier effect part 2: From microscopic to macroscopic behaviour. *Mater. Sci. Eng. A* **1996**, *207*, 216–223. [[CrossRef](#)]
29. Hähner, P.; Ziegenbein, A.; Rizzi, E.; Neuhäuser, H. Spatiotemporal analysis of Portevin-Le Chatelier deformation bands: Theory, simulation, and experiment. *Phys. Rev. B* **2002**, *65*, 134109. [[CrossRef](#)]
30. Bross, S.; Hähner, P.; Steck, E.A. Mesoscopic simulations of dislocation motion in dynamic strain ageing alloys. *Comput. Mater. Sci.* **2003**, *26*, 46–55. [[CrossRef](#)]

31. Kubin, L.P.; Estrin, Y. Evolution of dislocation densities and the critical conditions for the Portevin-Le Chatelier effect. *Acta Metall. Mater.* **1990**, *38*, 697–708. [[CrossRef](#)]
32. Fritsch, S.; Scholze, M.; Wagner, M.F.X. Influence of thermally activated processes on the deformation behavior during low temperature ECAP. *IOP Conf. Ser. Mater. Sci. Eng.* **2016**, *118*, 012030. [[CrossRef](#)]
33. Härtel, M.; Wagner, S.; Frint, P.; Wagner, M.F.X. Effects of particle reinforcement and ECAP on the precipitation kinetics of an Al-Cu alloy. *IOP Conf. Ser. Mater. Sci. Eng.* **2014**, *63*, 012080. [[CrossRef](#)]
34. Härtel, M.; Frint, P.; Abstoss, K.G.; Wagner, M.F.-X. Effect of Creep and Aging on the Precipitation Kinetics of an Al-Cu Alloy after One Pass of ECAP. *Adv. Eng. Mater.* **2017**, *1700307*, 1700307. [[CrossRef](#)]
35. Wagner, S.; Siebeck, S.; Hockauf, M.; Nestler, D.; Podlesak, H.; Wielage, B.; Wagner, M.F.X. Effect of SiC-reinforcement and equal-channel angular pressing on microstructure and mechanical properties of AA2017. *Adv. Eng. Mater.* **2012**, *14*, 388–393. [[CrossRef](#)]
36. McCormick, P.G. Theory of flow localisation due to dynamic strain ageing. *Acta Metall.* **1988**, *36*, 3061–3067. [[CrossRef](#)]
37. Balík, J.; Lukáč, P.; Kubin, L.P. Inverse critical strains for jerky flow in Al-Mg alloys. *Scr. Mater.* **2000**, *42*, 465–471. [[CrossRef](#)]
38. Picu, R.C.; Vincze, G.; Ozturk, F.; Gracio, J.J.; Barlat, F.; Maniatty, A.M. Strain rate sensitivity of the commercial aluminum alloy AA5182-O. *Mater. Sci. Eng. A* **2005**, *390*, 334–343. [[CrossRef](#)]
39. Schmahl, W.W.; Khalil-Allafi, J.; Hasse, B.; Wagner, M.; Heckmann, A.; Somsen, C. Investigation of the phase evolution in a super-elastic NiTi shape memory alloy (50.7 at.%Ni) under extensional load with synchrotron radiation. *Mater. Sci. Eng. A* **2004**, *378*, 81–85. [[CrossRef](#)]
40. Cai, Y.; Zhang, Q.; Yang, S.; Fu, S.; Wang, Y. Experimental Study on Three-Dimensional Deformation Field of Portevin-Le Chatelier Effect Using Digital Image Correlation. *Exp. Mech.* **2016**, *56*, 1243–1255. [[CrossRef](#)]
41. Schäfer, A.; Wagner, M.F.-X.; Pelegrina, J.L.; Olbricht, J.; Eggeler, G. Localization events and microstructural evolution in ultra fine grained NiTi shape memory alloys during thermo-mechanical loading. *Adv. Eng. Mater.* **2010**, *12*, 453–459. [[CrossRef](#)]
42. Delpueyo, D.; Balandraud, X.; Grédiac, M. Calorimetric signature of the Portevin-Le Chatelier effect in an aluminum alloy from infrared thermography measurements and heat source reconstruction. *Mater. Sci. Eng. A* **2016**, *651*, 135–145. [[CrossRef](#)]
43. Elibol, C.; Wagner, M.F.-X. Investigation of the stress-induced martensitic transformation in pseudoelastic NiTi under uniaxial tension, compression and compression-shear. *Mater. Sci. Eng. A* **2004**, *621*, 76–81. [[CrossRef](#)]
44. Le Cam, J.-B.; Robin, E.; Leotoing, L.; Guines, D. Calorimetric analysis of Portevin-Le Chatelier bands under equibiaxial loading conditions in Al-Mg alloys: Kinematics and mechanical dissipation. *Mech. Mater.* **2017**, *105*, 80–88. [[CrossRef](#)]
45. Zdunek, J.; Płowiec, J.; Sychalski, W.L.; Mizera, J. Acoustic emission studies of the Portevin-Le Chatelier effect in Al-Mg-Mn (5182) alloy. *Inż. Mater.* **2011**, *32*, 889–894.
46. Chemelik, F.; Ziegenbein, A.; Neuhauser, H.; Lukac, P. Investigating the Portevin-Le Chatelier effect by the acoustic emission and laser extensometry techniques. *Mater. Sci. Eng. A* **2002**, *324*, 200–207. [[CrossRef](#)]
47. Wevers, M. Listening to the sound of materials: Acoustic emission for the analysis of material behaviour. *NDT E Int.* **1997**, *30*, 99–106. [[CrossRef](#)]
48. Estrin, Y.; Lebyodkin, M.A. The influence of dispersion particles on the Portevin-Le Chatelier effect: From average particle characteristics to particle arrangement. *Mater. Sci. Eng. A* **2004**, *387–389*, 195–198. [[CrossRef](#)]
49. Thevenet, D.; Mliha-Touati, M.; Zeghloul, A. The effect of precipitation on the Portevin-Le Chatelier effect in an Al-Zn-Mg-Cu alloy. *Mater. Sci. Eng. A* **1999**, *266*, 175–182. [[CrossRef](#)]
50. McCormick, P.G. A model for the Portevin-Le Chatelier effect in substitutional alloys. *Acta Metall.* **1972**, *20*, 351–354. [[CrossRef](#)]
51. Beukel, A. Theory of the effect of dynamic strain aging on mechanical properties. *Phys. Status Solidi* **1975**, *30*, 197–206. [[CrossRef](#)]
52. Mulford, R.A.; Kocks, U.F. New observations on the mechanisms of dynamic strain aging and of jerky flow. *Acta Metall.* **1979**, *27*, 1125–1134. [[CrossRef](#)]
53. Lebyodkin, M.; Dunin-Barkowskii, L.; Bréchet, Y.; Estrin, Y.; Kubin, L.P. Spatio-temporal dynamics of the Portevin-Le Chatelier effect: Experiment and modelling. *Acta Mater.* **2000**, *48*, 2529–2541. [[CrossRef](#)]

54. Staab, T.E.M.; Haaks, M.; Modrow, H. Early precipitation stages of aluminum alloys-The role of quenched-in vacancies. *Appl. Surf. Sci.* **2008**, *255*, 132–135. [[CrossRef](#)]
55. Sauvage, X.; Wilde, G.; Divinski, S.V.; Horita, Z.; Valiev, R.Z. Grain boundaries in ultrafine grained materials processed by severe plastic deformation and related phenomena. *Mater. Sci. Eng. A* **2012**, *540*, 1–12. [[CrossRef](#)]
56. Kim, W.J.; Chung, C.S.; Ma, D.S.; Hong, S.I.; Kim, H.K. Optimization of strength and ductility of 2024 Al by equal channel angular pressing (ECAP) and post-ECAP aging. *Scr. Mater.* **2003**, *49*, 333–338. [[CrossRef](#)]
57. Divinski, S.V.; Reglitz, G.; Rösner, H.; Estrin, Y.; Wilde, G. Ultra-fast diffusion channels in pure Ni severely deformed by equal-channel angular pressing. *Acta Mater.* **2011**, *59*, 1974–1985. [[CrossRef](#)]
58. Schwink, C.; Nortmann, A. The present experimental knowledge of dynamic strain ageing in binary f.c.c. solid solutions. *Mater. Sci. Eng. A* **1997**, *234–236*, 1–7. [[CrossRef](#)]
59. Chihab, K.; Estrin, Y.; Kubin, L.P.; Vergnol, J. The kinetics of the Portevin-Le Chatelier bands in an Al-5at%Mg alloy. *Scr. Metall.* **1987**, *21*, 203–208. [[CrossRef](#)]
60. Ling, C.P.; McCormick, P.G. Strain rate sensitivity and transient behaviour in an Al-Mg-Si alloy. *Acta Metall. Mater.* **1990**, *38*, 2631–2635. [[CrossRef](#)]



© 2018 by the authors. Licensee MDPI, Basel, Switzerland. This article is an open access article distributed under the terms and conditions of the Creative Commons Attribution (CC BY) license (<http://creativecommons.org/licenses/by/4.0/>).